Monitoring Bridge Vibrations Based on GBSAR and Validation by High-Rate GPS Measurements

Yan Zhu, Bing Xu, Zhiwei Li, Jingxin Hou, and Qijie Wang

***Abstract*—Ground-Based synthetic aperture radar (GBSAR) is a novel technique for monitoring surface deformation and structural vibrations due to its unique advantages: GBSAR can continually and simultaneously observe a large range of landscapes with a high spatiotemporal resolution. Using GBSAR under the fixed azimuth scanning mode to monitor vibrations is a promising way to monitor a bridge's structural health. Several GBSAR-based bridge vibration experiments have been conducted and verified; however, observation precision tests using high-rate global positioning system (GPS) data are rare, especially for the GAMMA portable radar interferometer II (GPRI-II). In addition, it is complicated to split high-frequency signals into valuable information and undesired noise. Considering these limitations, an on-site experiment using the GPRI-II and high-rate GPS receivers was conducted to evaluate the utility of the GPRI-II. Moreover, a denoising method based on the least-squares adjustment and a triangular chain is proposed under the assumption that the atmospheric phase delay can be eliminated between minuscule time intervals. In addition, an external comparative experiment between the GPRI-II and GPS receivers and an internal comparative experiment was performed to evaluate the effectiveness and reliability, respectively, of the proposed method. The results show that the GPRI-II observation accuracy for permanent scatterers reaches 5–6 millimeters. For the effectiveness of the proposed method, the precision improvement for distributed scatterers is more significant than that for permanent scatterers, and both the internal precision and the external precision have more conspicuous relationships with the deviation of the amplitude than with the coherence.**

***Index Terms*—Denoising, ground-based synthetic aperture radar (GBSAR), global positioning system (GPS), high-frequency.**

I. Introduction

BRIDGES, as vital components of any national infrastructure, play important roles in cities worldwide by supporting people's lives and countries' economies. However, bridges suffer from deformation, aging, and damage that occur because of the structural design, construction flaws, and the influences of surrounding construction, loadings, and natural disasters, such as earthquakes and typhoons. Therefore, structural health monitoring (SHM) for bridges is crucial. A bridge SHM system is based on the real-time monitoring of environmental vibrations and the identification of damage [1], the information of which helps examine and maintain the bridge, thereby ensuring its structural stability.

Currently, dynamic testing under an environmental excitation is a common method for obtaining the dynamic responses of structures. According to the types of equipment used, the dynamic testing technique is classified into two categories, namely, contact and noncontact. Contact equipment includes accelerometers [2], linear variable differential transformers [3], global navigation satellite system (GNSS) receivers [4], fiber optic sensors [5], etc., which are directly installed on or inside the structure to measure vibrations. Noncontact equipment includes laser Doppler vibrometers (LDVs) [6], robotic total stations (RTSs) [7], ground-based synthetic aperture radar (GBSAR) [8], and high-speed cameras [9], and all of the installation (unlike that of contact equipment) is not complicated or dangerous because the sensors are located far from the structure. However, these noncontact devices are applied in different situations and have their own advantages and disadvantages. For instance, an LDV has an observation accuracy reaching between 0.1 and 0.2 mm and can measure the vibrations at different points, but LDVs are difficult to install beneath long-span bridges. As an alternative, an RTS is installed easily and has an observation accuracy of approximately 1–1.5 mm [7] but is limited by a low observation frequency and sparsity of measuring points [10]. The high-speed camera and video analysis technique has a submillimeter accuracy but similarly observes only a few points [9]. In contrast to the above, GBSAR has numerous advantages, that is, a large observation range, a high density of measuring points, a high frequency and accuracy, and simple installation.

Spaceborne interferometric synthetic aperture radar (InSAR) has been shown to display an outstanding ability to monitor the deformation caused by landslides [11]–[17] based on the characteristics of all-day and all-weather observations. Compared with spaceborne InSAR, GBSAR can be installed at an optimal location free of limitations to observe a scenario from an angle set by the user [18]. Benefitting from the flexibility of the observation angle, the deformations in multiple directions can be obtained. Thus, as a supplement to the spaceborne SAR, GBSAR has shown excellent superiority in monitoring the deformation

Manuscript received January 10, 2021; revised April 18, 2021; accepted May 18, 2021. Date of publication May 25, 2021; date of current version June 9, 2021. This work was supported in part by the National Science Fund for Distinguished Young Scholars under Grant 41925016, in part by the National Natural Science Foundation of China under Grant 41804008, and in part by the Innovation Foundation for Postgraduate of Central South University under Grant 2020zzts191. *(Corresponding author: Bing Xu.)*

Yan Zhu, Jingxin Hou, and Qijie Wang are with the School of Geosciences and Info-Physics, Central South University, Changsha 410083, China (e-mail: yanzhu@csu.edu.cn; houjingxin@csu.edu.cn; qjwang@csu.edu.cn).

Bing Xu and Zhiwei Li are with the School of Geosciences and Info-Physics, Central South University, Changsha 410083, China, with the Key Laboratory of Metallogenic Prediction of Nonferrous Metals and Geological Environment Monitoring Ministry of Education, School of Geoscience and Info-physics, Central South University, Changsha 410083, China, and also with the Hunan Key Laboratory of Nonferrous Resources and Geological Hazards Exploration, Changsha 410083, China (e-mail: xubing@csu.edu.cn; zwli@csu.edu.cn).

Digital Object Identifier 10.1109/JSTARS.2021.3083494

of dams [19], slopes [20]–[22], glaciers [23], [24], and structures [8], [25] according to its unique characteristics, namely, a high spatiotemporal resolution, the ability to acquire observations in real time, and high measuring accuracy. Additionally, based on its image-forming principle, ground-based radar is classified into two categories: GBSAR and ground-based real aperture radar.

The GAMMA portable radar interferometer II (GPRI-II) developed by GAMMA Remote Sensing and Consulting AG and used for this research is a rotating real aperture radar interferometer based on a frequency modulated continuous wave (FMCW) radar. The GPRI-II with a millimeter-level accuracy has been applied to multiple kinds of research [26], [27]. The maximum sampling frequency under fixed azimuth scanning (FAS) mode can reach up to 2000 Hz, which is an invaluable advantage over other devices.

In truth, the cross-comparisons of measurements acquired by GBSAR and other conventional methods are rare, and the comparative experiments to demonstrate the high-frequency performance of GBSAR are less. Some have been carried out, but these experiments could be polished. For example, Peduto implemented a cross-comparison of GBSAR displacement data and topographic measurements and resulted in matching well [28], which paid more attention to a far lower temporal resolution than ours. Zhang validated GBSAR observations by statistically analyzing historical GPS measurements [29]. In addition, Hu compared GBSAR measurements with GPS measurements, revealing inconsistencies in the time domain [30]. Hence, to validate the observation accuracy of the GPRI-II, it is deployed to monitor the vibrations of two long-span bridges in Changsha, China, and the observations are compared with the measurements of high-rate GPS receivers. Moreover, to extract the high-frequency information from the high-frequency signal and remove noise, we propose a method based on a triangular chain to denoise the signal instead of using a frequency-domain method, for example, the fast Fourier transform [31] or discrete wavelet transform [32], because it is difficult to distinguish two similar high-frequency tones in the frequency domain. The remainder of this article is organized as follows. In the II section, we introduce how to capture and process the data, including the ranging principle of the chirp. We propose a denoising method based on the least-squares (LS) method and a triangular chain. Then, we present the study area and equipment parameters and display the results in Section III. Finally, we analyze and discuss the results and draw our conclusions in Sections IV and V, respectively.

II. Data Acquisition and a New Processing Method

A. Principle of Acquiring FMCW Radar Data

The signal transmitted by an FMCW radar is called a "chirp," a sinusoidal wave whose frequency increases linearly with time(showed in Fig. 1). The radar continuously transmits N electromagnetic pulses for the duration of the chirp T_s. The frequency of the chirp increases at a constant step Δf, forming an effective bandwidth (the frequency range of radar emission and reception) $B = (N-1)\,\Delta f$.

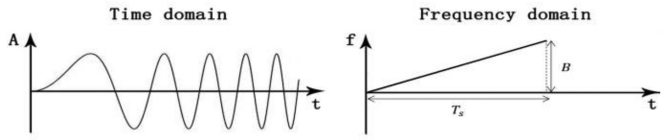

Fig. 1. A chirp represented in the time domain (left) and frequency domain (right).

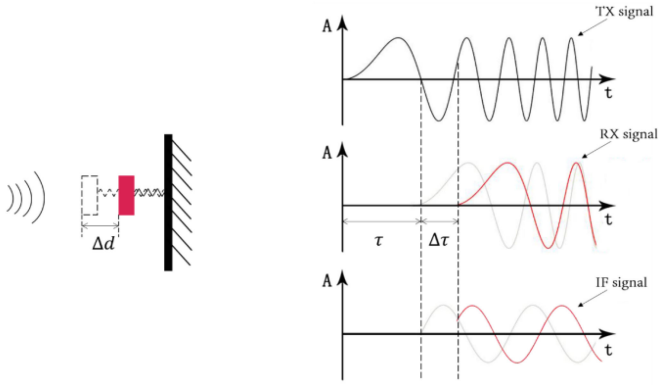

Fig. 2. A chirp represented in the time domain (left) and frequency domain (right).

Fig. 2 illustrates the principle of how an FMCW radar instrument monitors displacement. An intermediate frequency (IF) signal is generated by mixing the transmitted and received signals; thus, the IF is a constant value f equal to the difference between the instantaneous frequencies of the transmitted and received signals, and the intermediate phase ϕ is equal to the difference between their phases. The range d between the radar and an object is calculated by the phase difference and the time interval τ between the two signals. A time delay $\Delta\tau$ and phase delay $\Delta\phi$ will be recorded if a displacement has occurred with the relationship $\Delta\phi = 2\pi f\Delta\tau = 4\pi\Delta d/\lambda$.

B. New Processing Method Based on LS Adjustment and a Triangular Chain

The GPRI-II has two working modes, rotation azimuth scanning (RAS) and FAS, which results in different types of imaging geometries and corresponds to different data processing methods. In particular, the FAS mode is suitable to monitor the vibration of bridges. For the RAS mode, the data processing method is like that of satellite SAR data because of the similar 2-D imaging geometry. However, the FAS mode is easier to implement than the RAS mode due to the 1-D imaging geometry in the line-of-sight (LOS) direction. Moreover, in the RAS mode, the instrument takes considerable time to rotate, which reduces the temporal sampling rate. Because the vertical vibration component and high-frequency information are expected, the FAS mode is more suitable to record continuous observations over long intervals.

Some processing steps need to be emphasized. First, to improve the signal-to-noise ratio (SNR), decimation is applied to

the acquired raw data in the time domain. In this study, the chirp duration is set as 0.5 ms, and the decimation factor is set as 20. The frequency of the generated single look complex (SLC) image is 100 Hz, which is higher than that (50 Hz) of the GPS receivers used for the comparison test. Second, because of the imaging geometry and zero baseline configuration, the interferogram can be obtained directly without image coregistration or removing the flatten and topography phases, which are represented in (1). Note that the stable range profile is a preferential choice to be used as the reference. If required, a complex network helps reduce the atmospheric delay and phase noise. Third, because of the very high temporal resolution (500 μs) in the FAS mode, the interferometric phase can be unwrapped in the time domain, which is similar to that in the spatial domain. Finally, owing to the two receiving antennas, if required, the interferometric phase can be integrated by the upper and lower antennas (LAs) [28].

As shown in (1), the interferometric phase contains a deformation phase, an atmospheric delay phase, and a noise phase. Phase filtering is a conventional way to remove noise from the signal; however, as this approach will also filter out the high-frequency information we are interested in, a more rigorous method is needed

$$\phi_{\text{int}} = \varphi_1 \ - \ \varphi_2 = \phi_{\text{def}} \ + \phi_{\text{atm}} + \phi_{\text{noise}}. \tag{1}$$

To separate high-frequency information from noise, a denoising method based on the LS method and a triangular chain is proposed. Considering the minuscule time interval, we assume that the interferometric phases of adjacent acquisitions contain the deformation phase and noise only. Then, under the assumption that the noise is subject to a Gaussian distribution, the noise can be reduced by the LS adjustment. There are many network configurations for generating a series of interferometric phases; here, to decrease the propagation of error and avoid phase jumps, we choose the two-connection network chronologically.

Given *N* range profiles, the number of interferometric pairs is $M \ = \ 2N - 3$ because of the two-connection network chronologically. The SLC phase at the *m*th point on the *i*th range profile is defined as S_i^m, and the interferometric phase at the *m*th point on the range profile is $\phi_{i,j}^m (i < j$ and $i, j \in [1, N])$, which is obtained by the conjugate multiplication of S_i^m and S_j^m. The observation vector is $\boldsymbol{L} \ = [\phi_{1,2}, \phi_{1,3}, \phi_{2,3}, \ldots, \phi_{N-1,N}]^T$. The unknown vector is $\boldsymbol{x} \ = [\varphi_1, \varphi_2, \varphi_3, \ldots, \varphi_N]^T$, which refers to the adjusted SLC phase. Then, the relationship between the observation vector and the unknown vector is as follows:

$$\boldsymbol{L} \ = \ \boldsymbol{B}\boldsymbol{x} \tag{2}$$

where the design matrix $\boldsymbol{B}$ is a sparse matrix of size $M \times N$, in which the nonzero elements are given by $\boldsymbol{B}\,(k, i) = \ -1$ and $\boldsymbol{B}\,(k, i) = \ 1$, with k being the index of the range profile pairs and $k \in [1, M]$. The design matrix $\boldsymbol{B}$ with $M \times N$ is

$$B \ = \begin{bmatrix} -1 & 1 & 0 & \ldots & 0 & 0 \\ -1 & 0 & 1 & \ldots & 0 & 0 \\ 0 & -1 & 1 & \ldots & 0 & 0 \\ \vdots & \vdots & \vdots & \ddots & 1 & 0 \\ 0 & 0 & 0 & \cdots & -1 & 1 \end{bmatrix}. \tag{3}$$

Then, (2) is rewritten as the error equation

$$\boldsymbol{V} \ = \ \boldsymbol{B}\hat{\boldsymbol{x}} - \boldsymbol{L} \tag{4}$$

where $\hat{\boldsymbol{x}} = \ \boldsymbol{x} - \boldsymbol{x}^0$ and $\boldsymbol{x}^0$ refers to the approximate value of $\boldsymbol{x}$. Based on the weighted LS principle, we obtain the following equation:

$$\hat{\boldsymbol{x}} = \boldsymbol{G}^{-1} \ \boldsymbol{B}^T \boldsymbol{P}\boldsymbol{L} \,\text{with}\, \boldsymbol{G} \ = \boldsymbol{B}^T \boldsymbol{P}\boldsymbol{B} \tag{5}$$

where the matrix $\boldsymbol{P}$ is the weight matrix of observations and can be defined by the coherence of interferometric pairs:

$$\boldsymbol{P} \ = \ \text{diag}\left(|\gamma_1|, |\gamma_2|, \ldots, |\gamma_M|\right) \tag{6}$$

$$\gamma_k = \sum_{n=1}^{N} s_{in} s_{jn}^* \Big/ \sqrt{\sum\nolimits_{n=1}^{N} |s_{in}|^2 \cdot \sum\nolimits_{n=1}^{N} |s_{jn}|^2}. \tag{7}$$

Unfortunately, the design matrix $\boldsymbol{B}$ is column rank-deficient; therefore, $\boldsymbol{G}$ is a singular matrix in (5). To obtain a unique solution, we apply a weighted minimum-norm constraint to the solution, $\hat{\boldsymbol{x}}^T \boldsymbol{P}_x \ \hat{\boldsymbol{x}} = \ \mathbf{min}$. Considering that the matrix $\boldsymbol{G}$ in (5) is row rank-deficient, we can decompose the matrix into

$$\begin{cases} \boldsymbol{G}_1 \hat{\boldsymbol{x}} - \ \boldsymbol{L}_1 = \ 0 \\ \boldsymbol{G}_2 \hat{\boldsymbol{x}} - \ \boldsymbol{L}_2 = \ 0 \end{cases} \tag{8}$$

where $R\ (\boldsymbol{G}_1) = \ N - 1$. Let the first equation be a condition equation; then, build a new function $\boldsymbol{f}$, and make the first-order partial derivative with respect to $\hat{\boldsymbol{x}}$ zero

$$\boldsymbol{f} = \hat{\boldsymbol{x}}^T \ \boldsymbol{P}_x \hat{\boldsymbol{x}} - 2\boldsymbol{K}^T \ (\boldsymbol{G}_1 \hat{\boldsymbol{x}} - \boldsymbol{L}_1) \qquad = \ \min \tag{9}$$

$$\frac{\partial \boldsymbol{f}}{\partial \hat{\boldsymbol{x}}} = \ 2\hat{\boldsymbol{x}}^T \boldsymbol{P}_x - 2\boldsymbol{K}^T \ \boldsymbol{G}_1 = \ 0 \tag{10}$$

where $-2\boldsymbol{K}^T$ is the Lagrangian multiplier. Then, we can obtain

$$\hat{\boldsymbol{x}} = \boldsymbol{P}_x^{-1} \ \boldsymbol{G}_1^T \boldsymbol{K} \ = \boldsymbol{Q}_x \ \boldsymbol{G}_1^T \boldsymbol{K}. \tag{11}$$

Replacing the first equation in (8) with (11), the normal equation is obtained:

$$\boldsymbol{G}_1 \boldsymbol{Q}_x \boldsymbol{G}_1^T \boldsymbol{K} - \ \boldsymbol{L}_1 = \ 0 \tag{12}$$

$$\boldsymbol{K} \ = \left(\boldsymbol{G}_1 \boldsymbol{Q}_x \boldsymbol{G}_1^T\right)^{-1} \ \boldsymbol{L}_1 = \tilde{\boldsymbol{Q}}_x \ \boldsymbol{L}_1. \tag{13}$$

Substituting $\boldsymbol{K}$ into (11) yields

$$\hat{\boldsymbol{x}} = \boldsymbol{Q}_x \ \boldsymbol{G}_1^T \tilde{\boldsymbol{Q}}_x \boldsymbol{L}_1. \tag{14}$$

Note that $\boldsymbol{P}_x$ as a prior weight matrix represents the stability of unknowns in $\boldsymbol{x}$. In this study, we denote the local SNR as the prior weight of the unknowns. The local SNR is the ratio of

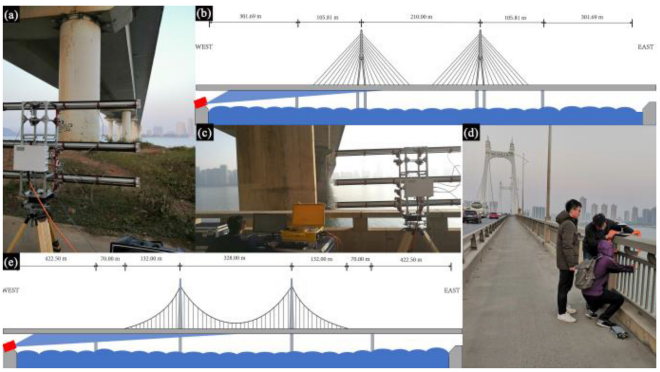

Fig. 3. (a) and (c) In situ measurement setup. (d) GPS receiver being installed on the bridge balustrade. (b) and (c) Sketches of the Yinpenling Bridge and Sanchaji Bridge, respectively.

the phase standard deviation in a local window to the maximum phase standard deviation in the range profile [33]

$$\sigma_{\varphi} = \left(\left(\sum_{N} \left(\varphi\left(p,q\right) - \bar{\varphi}\left(p,q\right) \right)^2 \right) / \left(N-1\right) \right)^{1/2} \tag{15}$$

$$\mathrm{SNR} = 10\log_{10}\left(\sigma^2_{\varphi,\max}/\sigma^2_{\varphi}\right) \tag{16}$$

where $\log_{10}()$ represents the common logarithm function with the base of 10. Then, we normalize all the SNRs in the time domain at the same point to obtain the prior weight:

$$\boldsymbol{P}_x = \frac{\mathrm{SNR}}{\max\left(\mathrm{SNR}\right)}. \tag{17}$$

Note that the values of N in (7) and (15) refer to the size of the estimation window instead of the number of range profiles.

III. Experiment and Results

A. Study Area

In this section, we describe experimental observations of two long-span bridges, namely, the Yinpenling Bridge and Sanchaji Bridge, both of which are located in the northern Changsha and connect Yuelu District with Kaifu District.

The Yinpenling Bridge is a long-span prestressed cable-stayed bridge with a total length of 3616 m; the length of the main bridge is 1025 m, and the width is 25 m. The two towers standing in the middle are 210 m apart with a height of 53.72 m (see Fig. 3). As a significant transport infrastructure downtown, this bridge carries only cars and buses.

The Sanchaji Bridge is a paired-tower three-span self-anchored suspension bridge with a total length of 1577 m. The length of the main bridge is 732 m, with two towers standing 328 m apart in the middle. The Sanchaji Bridge crosses the Xiangjiang River and supports freight traffic in the northern suburbs of Changsha.

In this study, the GPRI-II was deployed under both bridges on their western upstream sides. The equipment is composed of a fixing module, a transmitting and receiving module, and a controller. The fixing module includes a tripod, a pedestal, and an azimuth scanner with a tribrach. The transmitting and receiving module comprises an antenna tower, a radio frequency assembly, a transmit antenna, and two receive antennas, all of which are Ku-band V-polarized antennas. Table I shows the basic parameters of the GPRI-II. Three GNSS receivers, provided by Trimble Inc., were mounted on the bridges. The sampling frequency was set to 50 Hz. And the real-time kinematic solution mode was applied to monitor the vibration.

TABLE I
Basic Parameters of the GPRI-II

Parameter	Value
Radar type	FMCW
Antenna type	Slotted waveguide
Frequency range	17.1-17.3 GHz (Ku-band)
Bandwidth	200 MHz
Frequency accuracy	<100 Hz
Maximum sampling frequency	4000 Hz
Measurement range	50-10000 m
Azimuth beamwidth	0.385 deg (-3 dB)
Elevation beamwidth	35 deg (-3 dB)
Range sample spacing	0.75 m
Range resolution	0.95 m (-3 dB)
Azimuth resolution	6.8 m at 1 km (-3 dB)
Displacement accuracy	< 1 mm at 1 km
Time reference	UTC

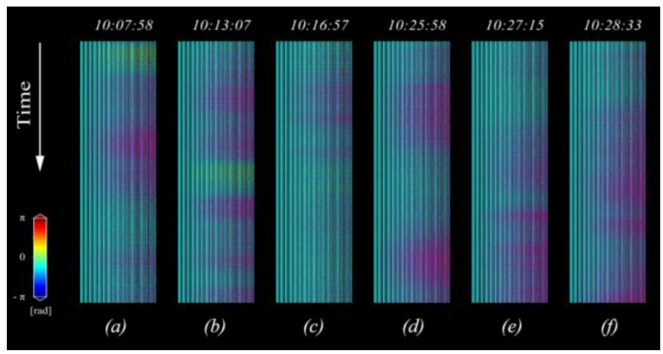

Fig. 4. (a)–(f) Six selected interferograms from the Sanchaji Bridge with an observation duration of 45 s.

B. Experimental Results

The first line was chosen as the reference range profile. Then, ordinary interferometry was implemented, and interferograms were obtained. Fig. 4 shows the interferograms acquired by the LA at the Sanchaji Bridge. Six interferograms were selected with starting times (in Universal Coordinated Time, UTC) of 10:07:58, 10:13:07, 10:16:57, 10:25:58, 10:27:15, 10:28:33 (the format is hh:mm:ss), and the observation duration was 45 s. The azimuth direction represents the temporal domain, and the resolution is 0.01 s. The range direction represents the spatial domain in the LOS direction, and the resolution is 0.75 m. Heavy trucks accounted for a large portion of the traffic on the Sanchaji Bridge, leading to significant deformations.

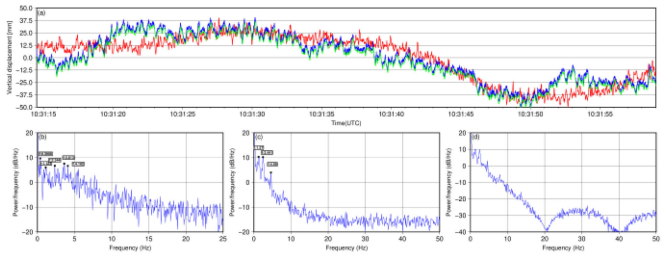

Fig. 5. (a) Comparison of the time series at 10:31:07. (b)–(d) PSDs of the GPS time series, GBSAR time series calculated by the proposed method, and GBSAR time series calculated by mean filtering, respectively, using the periodogram method.

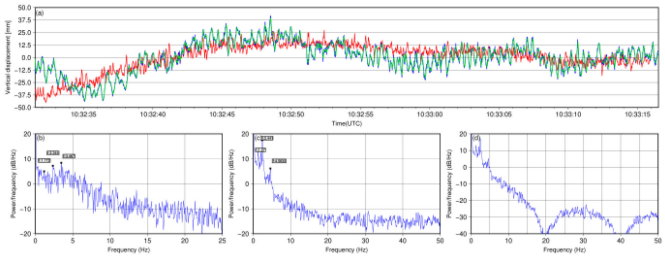

Fig. 6. (a) Comparison of the time series at 10:32:24. (b)–(d) PSDs of the GPS time series, GBSAR time series calculated by the proposed method, and GBSAR time series calculated by mean filtering, respectively, using the periodogram method.

IV. Analysis and Discussion

A. Frequency Comparison to the Mean Filtering Method

At first, the time series were transformed from the time domain to the frequency domain to validate the performance of preserving the high frequencies with the proposed method. The Welch method was implemented for the data acquired by the two monitoring systems to obtain the power spectral density (PSD). Additionally, the GBSAR time series acquired by mean filtering were compared. The filter was applied to each interferometric sequence before phase unwrapping. The Hamming window with a length of 1000, 66.6% of overlapping subsamples, and a discrete Fourier transform whose length is the next power of two greater than the length of the segments were applied to all of the time series. The Hamming window has a similar characteristic to the Hanning window, but further suppresses the first side lobe [34]. The frequency range varies from 0 to 100 for the GBSAR time series and from 0 to 50 for the GPS time series, while the frequency resolutions are $1/(1024 \times 0.01) = 0.0977$ for the GBSAR time series and $1/(\{1024 \times 0.02) = 0.0488$ for the GPS time series.

The time series acquired at 10:31:07 and 10:32:24 are shown and compared in both the time and the frequency domains in Figs. 5 and 6. In Figs. 5(a) and 6(a), the red polyline represents the GPS time series, the blue polyline represents the GBSAR time series calculated by the proposed method, the green polyline represents the GBSAR time series calculated by mean filtering, and their PSDs are shown in (b)–(d). In the time domain, the different methods for the GBSAR time series yield proximate results, and the observations acquired by the two types of systems have the same general trend, but there are still some partial inconsistencies. In the frequency domain, unlike the mean filtering approach, the proposed method leads to a result, which is similar to the GPS time series and preserves the high-frequency signal. We also calculated the RMSE of the GBSAR series obtained by the two methods. At the time 10:31:07, the RMSE is 11.29 for the time series obtained by the proposed method while it is 11.15 for that obtained by the mean filtering. At the time 10:32:24, the RMSE is 11.25 for the former while it is 11.13 for the latter. The improvement is not significant, but our method reserves the high-frequency signal.

TABLE II
Comparison of the Frequency Values Corresponding to Obvious PSD Peaks

Time	Device	1	2	3	4	5
10:31:07	GBSAR	1.27	2.441	4.59		
	GPS	0.3906	1.123	2.344	3.613	4.102
10:32:24	GBSAR	1.27	2.441	4.59		-
	GPS	1.172	2.344	3.467		-

For both systems, the frequency values corresponding to obvious PSD peaks are approximate but not identical, which is showed in Table II. We hypothesize that wind influenced the GPS receivers, introducing noise that explains the disagreement (that is, the similar trends in the time domain but the different values in the frequency domain). Additionally, the vibration of the balustrade caused by wind is another reason for this deviation.

B. Precision Validation by an Internal Comparison

To evaluate the reliability of our method, an internal comparison is implemented. First, decimation is performed. Under the assumption that the two line-adjacent observations have only minor differences, and an original SLC image with N lines is separated into two subimages, namely, an odd-numbered SLC image and an even-numbered SLC image. Each subimage is averaged by 10 lines, and then the average value is defined as the observation of this group. Therefore, two SLC images are obtained with $N/20$ lines and have the same frequency as the original SLC image with a decimation factor of 20. Fig. 7 illustrates the process of obtaining two decimated SLC images. Next, the proposed method is applied to the same bin in both resampled SLC images, resulting in two adjusted SLC phase time series. Finally, for the two adjusted SLC phase time series obtained from one original SLC dataset, the difference between them, namely, the internal difference, is calculated, and the standard deviation of the internal difference is defined as the internal precision representing the consistency of the results.

The internal comparison method mentioned above is applied to 40 original SLC data points observed by the two antennas during 20 acquisitions on the Sanchaji Bridge. The internal differences in the 327th, 516th, and 943rd bins for the upper and LAs are shown in Figs. 8 and 9, respectively, in the form of frequency histograms, in which the range is limited to between -1 and 1 rad (equal to 0.138 cm); the average values of the

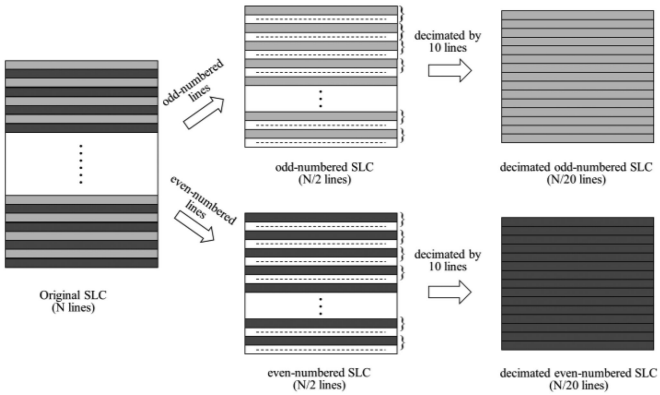

Fig. 7. Process of obtaining a decimated odd-numbered SLC image and a decimated even-numbered SLC image.

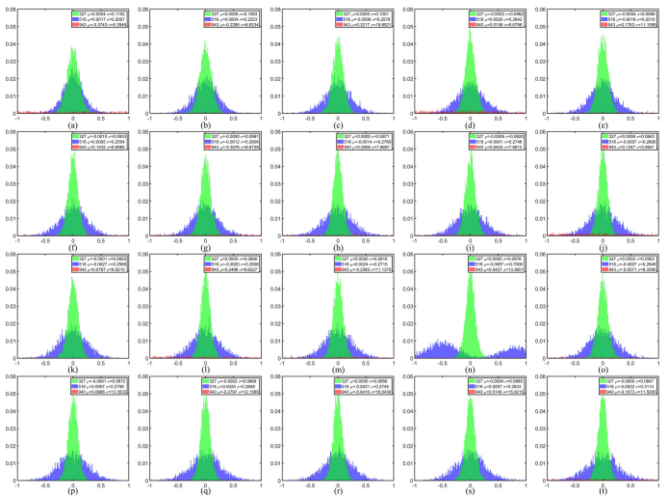

Fig. 8. Frequency histograms of the internal differences for the upper antenna, in which green represents the 327th bin, blue represents the 516th bin, and red represents the 943rd bin.

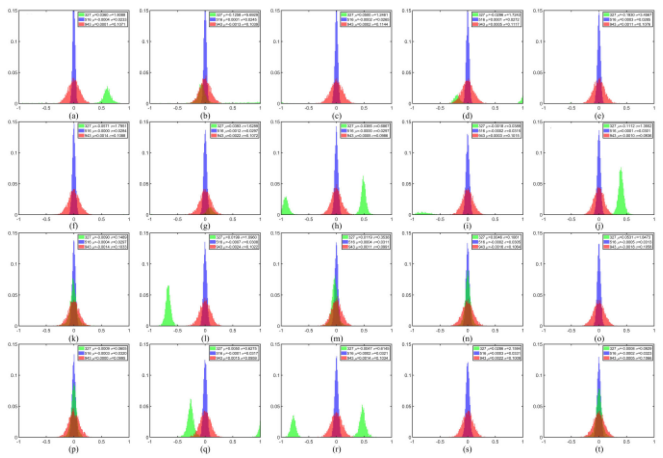

Fig. 9. Frequency histograms of the internal differences for the LA, in which green represents the 327th bin, blue represents the 516th bin, and red represents the 943rd bin.

TABLE III
INTERNAL PRECISION COMPARISON FOR THE SANCHAJI BRIDGE (UA: UPPER ANTENNA; LA: LOWER ANTENNA)

Bridge	Location	UA internal precision (rad)	LA internal precision (rad)
SCJ	327	0.09	1.38
	516	0.29	0.03
	943	10.39	0.1

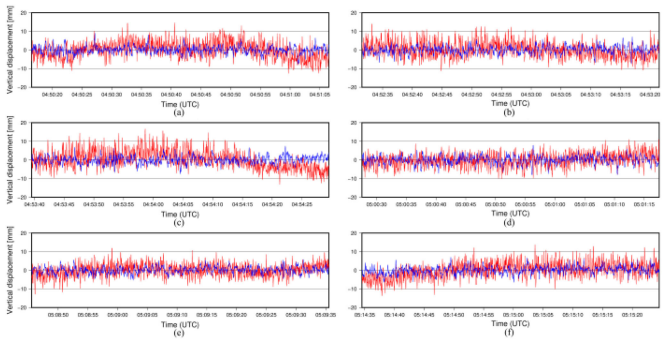

Fig. 10. Vertical deformation of the Yinpenling Bridge in the 219th bin in comparison with the GPS1 measurements. The red line represents the GPS time series, while the blue line represents the GBSAR time series.

internal precision are displayed in Table III. In Figs. 8 and 9, green represents the 327th bin, blue represents the 516th bin, and red represents the 943rd bin. For the upper antenna, the internal precision for the 327th bin is the best, while that for the 943rd bin is the worst; most of the internal differences for the 943rd bin are outside the range of -1 to 1 rad. For the LA, the internal precision for the 516th bin is the best, while that for the 327th bin is the worst; for the 327th bin, the internal precision for the upper antenna is better than that for the LA, but the opposite is true for the 516th and 943rd bins.

C. Accuracy Validation Via High-Rate GPS Measurements

Under the assumption that vertical vibrations constitute the main contribution for most bridges [29], the GBSAR observations are projected in the vertical direction according to the viewing geometry. For validation, three GPS receivers were installed on the balustrade at the Yinpenling Bridge. According to the imaging geometry of the GPRI-II, the three receivers (GPS1, GPS2, and GPS3) are projected onto the radar images in the 219th, 762nd, and 492nd bins, respectively. The selected time series are shown in Figs. 10–12 with the same observation durations, whose starting times (UTC) are 04:50:06, 04:52:22, 04:53:29, 05:00:17, 05:08:36, 05:14:28 (the format is hh:mm:ss). The red line represents the GPS time series, while the blue line represents the GBSAR time series. All of these time series have similar amplitudes and trends, but the observation frequency of GBSAR is higher than that of GPS, and both of them demonstrate that the deformation of the Yinpenling Bridge is relatively small in the range of plus or minus 20 mm. Similarly, three GPS receivers were installed on the balustrade

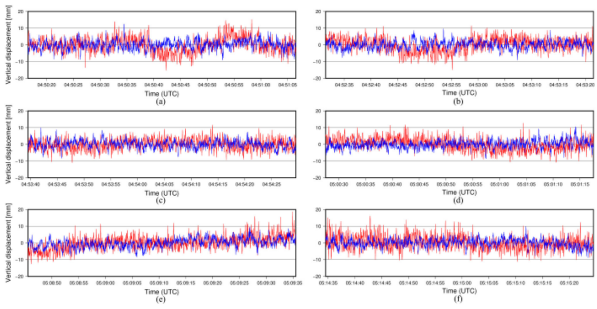

Fig. 11. Vertical deformation of the Yinpenling Bridge in the 762nd bin in comparison with the GPS2 measurements. The red line represents the GPS time series, while the blue line represents the GBSAR time series.

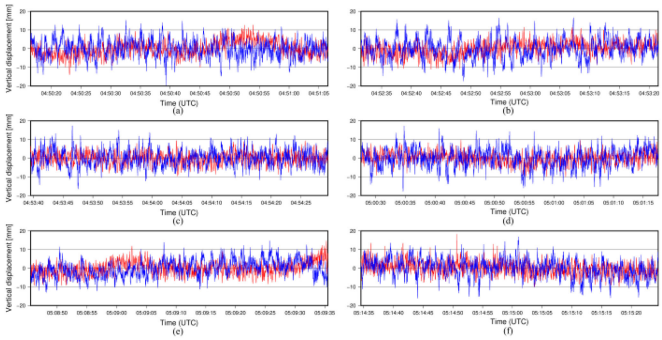

Fig. 12. Vertical deformation of the Yinpenling Bridge in the 492nd bin in comparison with the GPS3 measurements. The red line represents the GPS time series, while the blue line represents the GBSAR time series.

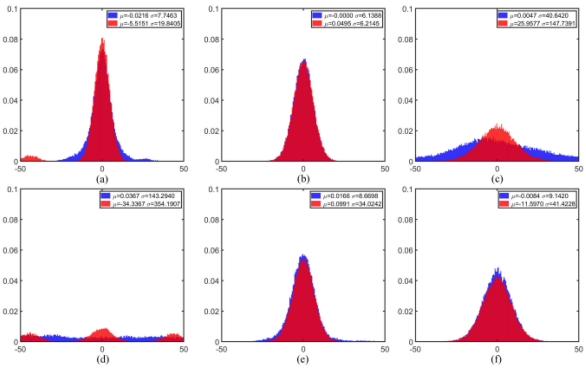

Fig. 13. Probability distribution diagrams of the differences between the GBSAR results and GPS observations. Blue values are calculated with the proposed method, while red values are calculated without this method. (a)–(c) Obtained by the upper antenna. (d)–(f) Obtained by the lower antenna. From left to right, the three columns correspond to the 219th, 492nd, and 762nd bins on the Yinpenling Bridge.

at the Sanchaji Bridge. GPS1, GPS2, and GPS3 are projected onto the radar images in the 327th, 516th, and 943rd bins, respectively. Note that, the average value of every time series is taken as the vibration reference value, under the assumption that the expectation of a time series corresponds to a stable state of a bridge. Therefore, the value that is proximate to the average is selected as the reference.

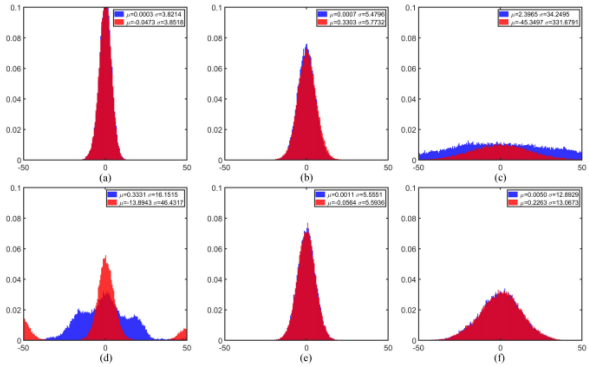

Fig. 14. Probability distribution diagrams of the differences between the GBSAR results and GPS observations. Blue values are calculated with the proposed method, while red values are calculated without this method. (a)–(c) Obtained by the upper antenna. (d)–(f) Obtained by the lower antenna. From left to right, the three columns correspond to the 327th, 516th, and 943rd bins on the Sanchaji Bridge.

TABLE IV
ACCURACY IMPROVEMENTS WITH THE PROPOSED METHOD (UA: UPPER ANTENNA; LA: LOWER ANTENNA)

Bridge	Loc.	UA latter RMSE (mm)	UA previous RMSE (mm)	Improvement rate	LA latter RMSE (mm)	LA previous RMSE (mm)	Improvement rate
YPL	219	7.75	19.84	60.94%	143.29	354.19	59.54%
	492	6.14	6.21	1.13%	8.67	34.02	74.51%
	762	40.64	147.74	72.49%	9.14	41.42	77.93%
SCJ	327	3.82	3.85	0.78%	16.15	46.43	65.22%
	516	5.48	5.77	5.03%	5.56	5.59	0.54%
	943	34.25	331.68	89.67%	12.89	13.07	1.38%

To evaluate the effectiveness of the proposed method, the GBSAR results were compared with the GPS observations. First, two types of GBSAR results were calculated: one set was obtained with the proposed method, and the other set was obtained without this method. Then, taking the GPS observations as the reference, the root mean square errors (RMSEs) were calculated for both types of GBSAR results. Considering that the frequency of the GPRI-II is twice that of a GPS receiver, the data series obtained by GBSAR was sampled. Table IV presents the RMSEs of the date sets calculated with and without our method in the 219th, 492nd, and 762nd bins on the Yinpenling Bridge and in the 327th, 516th, and 943rd bins on the Sanchaji Bridge. In general, the method proposed in this article yields a more obvious accuracy correction for the Yinpenling Bridge. The differences were counted in three bins for both antennas on the two bridges, and the corresponding probability distribution diagrams are displayed in Figs. 13 and 14, in which the range is limited to between −50 and 50 mm (the differences beyond this range are not shown in the figures).

D. Scattering Characteristics and Precision Improvement

The bins at different locations show different internal and external precisions. To investigate the reason for this discrepancy, at first, the average coherence (with an estimation window of

TABLE V
AVERAGE COHERENCE AND DA FOR THE YINPENLING AND SANCHAJI BRIDGES (UA: UPPER ANTENNA; LA: LOWER ANTENNA)

Bridge	Location	UA coherence	UA DA	LA coherence	LA DA
YPL	219	0.90	0.30	0.96	0.44
	492	0.99	0.26	0.98	0.29
	762	0.73	0.36	0.85	0.29
SCJ	327	0.98	0.19	0.73	0.36
	516	0.95	0.25	0.99	0.08
	943	0.73	0.38	0.97	0.16

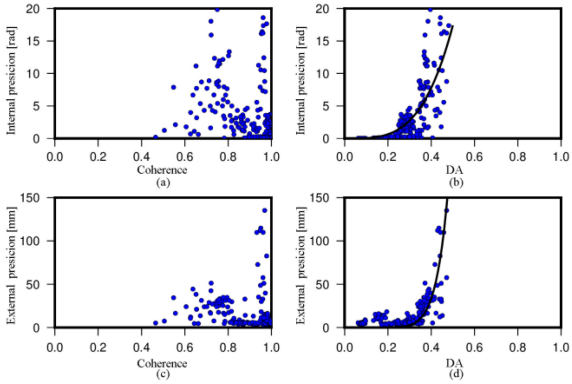

Fig. 15. Statistical results between the (a) internal precision and coherence, (b) internal precision and deviation of the amplitude (DA), (c) external precision and coherence, and (d) external precision and DA.

1×7) and DA were calculated in every bin for one duration. The average coherence and DA for the 17 time series on the Yinpenling Bridge and for the 20 time series on the Sanchaji Bridge are also shown in Table V. All the observations in the six bins were analyzed to explore the relationship between the measurement accuracy and the stability of the target, as shown in Fig. 15. Both the external precision and the internal precision decrease with the DA, which means that the more stable the target is, the more reliable the observation. Moreover, the measurement accuracy and DA exhibit a significant exponential correlation, and the relationship is stronger than that between the measurement accuracy and coherence. Both the internal precision and the external precision have more significant relationships with the DA than the coherence, suggesting that DA is a better index for representing a target's stability.

Then, combining Tables III and V, we will see that the more stable the target is, the better the internal precision. Compare Tables IV and V, and we can see that for distributed scatterers our method yields a more remarkable accuracy correction than permanent scatterers. For the 492nd pixel in the UA in YPL, and for the 327th pixel in the UA, the 516th pixel in the UA and LA, the 943rd pixel in the LA in the SCJ, this method has an insignificant impact on these fixed scatterers. However, for distributed scatterers, this method has a more significant improvement. In addition, for the 943rd pixel in the UA and the 327th pixel in the LA in SCJ, the improvement is significant but suspect because of their SNR according to their coherence and DA.

V. CONCLUSION

In this study, bridge vibrations were monitored by GBSAR, and the measurements were validated by GPS observations. Additionally, a denoising method based on the LS adjustment for GBSAR was proposed. This method analyses the phase contributions in the interferometric phase, mitigates the atmospheric delay, and extracts the high-frequency information from the noisy signal. Two comparative tests were conducted to examine the reliability and effectiveness of this method. The improvement for distributed scatterers is more significant than that for fixed scatterers with the proposed method. Both the internal precision and the external precision have more conspicuous relationships with the DA than the coherence. Additionally, as the statistical results show, the smaller the DA is, the higher the observation precision is, which is similar to the common sense with satellite SAR images. These findings show that the DA is a better index than coherence in the FAS mode to represent the stability of a target; hence, it is worth further investigating the influence on the phase stability by the incidence angle, the distance between the radar and the target, and targets' reflection characteristics. Furthermore, the experimental results for the Yinpenling Bridge and Sanchaji Bridge reveal that traffic loads and wind are the major factors causing bridges to vibrate, and the effect on the Sanchaji Bridge was more significant due to the passage of heavy trucks.

GBSAR is a promising technique for monitoring the vibrations of long-span bridges. Compared with traditional monitoring devices and technologies, GBSAR has numerous advantages, namely, a higher sampling frequency and a larger scope of simultaneous observations, which constitute substantial benefits for bridge SHM. However, monitoring by GBSAR requires rigorous constraints on the observation conditions, including the height between the equipment and the bottom surface of the bridge, the bridge structure, and the viewing angle.

REFERENCES

[1] K.-Y. Wong, "Design of a structural health monitoring system for long-span bridges," *Struct. Infrastruct. Eng.,* vol. 3, no. 2, pp. 169–185, 2007.
[2] J. W. Lee, J. D. Kim, C. B. Yun, J. H. Yi, and J. M. Shim, "Health-monitoring method for bridges under ordinary traffic loadings," *J. Sound Vib.*, vol. 257, no. 2, pp. 247–264, 2001.
[3] H. H. Nassif, M. Gindy, and J. Davis, "Comparison of laser doppler vibrometer with contact sensors for monitoring bridge deflection and vibration," *NDT E Int.*, vol. 38, no. 3, pp. 213–218, 2005.
[4] Y. L. Xu, B. Chen, C. L. Ng, K. Y. Wong, and W. Y. Chan, "Monitoring temperature effect on a long suspension bridge," *Struct. Control Health Monit.*, vol. 17, pp. 632–653, 2009.
[5] S. Sumitro and M. Wang, "Sustainable structural health monitoring system," *Struct. Control Health Monit.*, vol. 12, pp. 445–467, 2005.
[6] J. J. Lee and M. Shinozuka, "A vision-based system for remote sensing of bridge displacement," *NDT E Int.*, vol. 39, no. 5, pp. 425–431, 2006.
[7] P. A. Psimoulis and S. C. Stiros, "Measurement of deflections and of oscillation frequencies of engineering structures using robotic theodolites (RTS)," *Eng. Struct.*, vol. 29, no. 12, pp. 3312–3324, 2007.
[8] M. Pieraccini *et al.*, "Structural static testing by interferometric synthetic radar," *NDT E Int.*, vol. 33, no. 8, pp. 565–570, 2000.
[9] D. Ribeiro, R. Calçada, J. Ferreira, and T. Martins, "Non-contact measurement of the dynamic displacement of railway bridges using an advanced video-based system," *Eng. Struct.*, vol. 75, pp. 164–180, 2014.
[10] J. Yu, P. Zhu, B. Xu, and X. Meng, "Experimental assessment of high sampling-rate robotic total station for monitoring bridge dynamic responses," *Measurement,* vol. 104, pp. 60–69, 2017.

[11] X. M. Fan *et al.*, "Failure mechanism and kinematics of the deadly June 24th 2017 Xinmo landslide, Maoxian, Sichuan, China," *Landslides*, vol. 14, no. 6, pp. 2129–2146, Dec. 2017.
[12] E. Intrieri *et al.*, "The Maoxian landslide as seen from space: Detecting precursors of failure with Sentinel-1 data," *Landslides*, vol. 15, no. 1, pp. 123–133, Jan. 2018.
[13] S. Figueroa-Miranda, J. Tuxpan-Vargas, J. A. Ramos-Leal, V. M. Hernández-Madrigal, and C. I. Villaseñor-Reyes, "Land subsidence by groundwater over-exploitation from aquifers in tectonic valleys of central Mexico: A review," *Eng. Geol.*, vol. 246, pp. 91–106, 2018.
[14] W. B. Xu, Z. W. Li, X. L. Ding, C. C. Wang, and G. C. Feng, "Application of small baseline subsets D-InSAR technology to estimate the time series land deformation and aquifer storage coefficients of Los Angeles area," *Chin. J. Geophys.-Chin.*, vol. 55, no. 2, pp. 452–461, Feb. 2012.
[15] G. Herrera, R. Tomas, F. Vicente, J. M. Lopez-Sanchez, J. J. Mallorqui, and J. Mulas, "Mapping ground movements in open pit mining areas using differential SAR interferometry," *Int. J. Rock Mech. Mining Sci.*, vol. 47, no. 7, pp. 1114–1125, Oct. 2010.
[16] T. Strozzi, A. Kouraev, A. Wiesmann, U. Wegmüller, A. Sharov, and C. Werner, "Estimation of Arctic glacier motion with satellite L-band SAR data," *Remote Sens. Environ.*, vol. 112, no. 3, pp. 636–645, 2008.
[17] E. Chaussard, S. Wdowinski, E. Cabral-Cano, and F. Amelung, "Land subsidence in central Mexico detected by ALOS InSAR time-series," *Remote Sens. Environ*, vol. 140, pp. 94–106, 2014.
[18] O. Monserrat, M. Crosetto, and G. Luzi, "A review of ground-based SAR interferometry for deformation measurement," *ISPRS J. Photogramm. Remote Sens.*, vol. 93, pp. 40–48, 2014.
[19] D. Tarchi, H. Rudolf, G. Luzi, L. Chiarantini, P. Coppo, and A. J. Sieber, "SAR interferometry for structural changes detect ion a demonstration test on a dam," in *Proc. IGARSS*, 1999, pp. 1522–1524.
[20] D. Tarchi *et al.*, "Landslide monitoring by using ground-based SAR interferometry: An example of application to the tessina landslide in Italy," *Eng. Geol.*, vol. 68, no. 1, pp. 15–30, 2003.
[21] D. Tarchi *et al.*, "On the use of ground-based SAR interferometry for slope failure early warning: The cortenova rock slide (Italy)," in *Landslides: Risk Analysis and Sustainable Disaster Management*, K. Sassa, H. Fukuoka, F. Wang, and G. Wang, Eds. Berlin, Germany: Springer, 2005, pp. 337–342.
[22] G. Luzi *et al.*, "Advances in ground-based microwave interferometry for landslide survey: A case study," *Int. J. Remote Sens.,* vol. 27, no. 12, pp. 2331–2350, 2006.
[23] G. Luzi *et al.*, "Monitoring of an alpine glacier by means of ground-based SAR interferometry," *IEEE Geosci. Remote Sens. Lett.,* vol. 4, no. 3, pp. 495–499, Jul. 2007.
[24] L. Noferini, D. Mecatti, G. Macaluso, M. Pieraccini, and C. Atzeni, "Monitoring of Belvedere glacier using a wide angle GB-SAR interferometer," *J. Appl. Geophys.*, vol. 68, no. 2, pp. 289–293, 2009.
[25] D. Tarchi, E. Ohlmer, and A. Sieber, "Monitoring of structural changes by radar interferometry," *Res. Nondestruct. Eval.,* vol. 9, no. 4, pp. 213–225, 1997.
[26] C. Werner, T. Strozzi, A. Wiesmann, and U. Wegmuller, "A real-aperture radar for ground-based differential interferometry," in *Proc. IEEE Int. Geosci. Remote Sens. Symp.*, vol. 3, 2008, pp. III–210–III–213.
[27] C. Werner, A. Wiesmann, T. Strozzi, A. Kos, R. Caduff, and U. Wegmiüler, "The GPRI multi-mode differential interferometric radar for ground-based observations," in *Proc. 9th Eur. Conf. Synthetic Aperture Radar*, 2012, pp. 304–307.
[28] D. Peduto *et al.*, "Investigating the kinematics of the unstable slope of Barberà de la Conca (Catalonia, Spain) and the effects on the exposed facilities by GBSAR and multi-source conventional monitoring," *Landslides*, vol. 18, no. 1, pp. 457–469, 2020.
[29] B. Zhang *et al.*, "Dynamic displacement monitoring of long-span bridges with a microwave radar interferometer," *ISPRS J. Photogramm. Remote Sens.*, vol. 138, pp. 252–264, 2018.
[30] J. Hu, J. Guo, Y. Xu, L. Zhou, S. Zhang, and K. Fan, "Differential ground-based radar interferometry for slope and civil structures monitoring: Two case studies of landslide and bridge," *Remote Sens.*, vol. 11, no. 24, 2019, Art. no. 2887.
[31] R. Brincker, L. Zhang, and P. Andersen, "Modal identification of output only systems using frequency domain decomposition," *Smart Mater. Struct.*, vol. 10, 2001, Art. no. 441.
[32] M. Soltaninejad, S. Soroushian, and H. Livani, "Application of short-time matrix pencil method for high-frequency damage detection in structural system," *Struct. Control Health Monit.*, vol. 27, no. 8, p. 20, Aug. 2020, Art. no. e2589.
[33] Q. Sun, Z.-W. Li, J.-J. Zhu, X.-L. Ding, J. Hu, and B. Xu, "Improved goldstein filter for InSAR noise reduction based on local SNR," *J. Central South Univ.*, vol. 20, no. 7, pp. 1896–1903, 2013.
[34] D.-J. Jwo, W.-Y. Chang, and I. H. Wu, "Windowing techniques, the welch method for improvement of power spectrum estimation," *Comput., Mater. Continua*, vol. 67, no. 3, pp. 3983–4003, 2021.

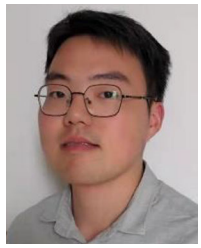

Yan Zhu received the bachelor's degree in surveying and mapping engineering from Central South University, Changsha, China, in 2018.

Since then, he has been with the Institute of Radar Remote Sensing & Imaging Geodesy (RRSIG), Central South University, Changsha, China. His studies regard interferometric synthetic aperture radar (InSAR). In particular, his main research interests include structure deformation monitoring, GBSAR, and the geological application of InSAR.

Bing Xu received the B.S. and Ph.D. degrees in geodesy and surveying engineering from Central South University, Hunan, China, in 2011 and 2016, respectively.

From June 2012 to June 2013, he was a Junior Research Assistant with the Institute of Space and Earth Information Science, the Chinese University of Hong Kong (CUHK), Shatin, Hong Kong. From June 2013 to January 2014, he was a Research Assistant with the Department of Land Surveying and Geo-Informatics, the Hong Kong Polytechnic University (HKPU), Kowloon, Hong Kong. He currently works with the Radar Group, the School of Geoscience and Info-Physics, Central South University, Changsha, China. His research interests include SAR big data processing and algorithm developments for multitemporal InSAR technique.

Zhiwei Li received the bachelor's and master's degrees in surveying engineering from the Central South University of Technology (now Central South University), Changsha, China, in 1997 and 1999, respectively, and the Ph.D. degree in remote sensing from The Hong Kong Polytechnic University, Kowloon, Hong Kong, in 2005.

He is currently a Full Professor with the Department of Surveying and Remote Sensing, School of Geosciences and Info-Physics, Central South University. He has authored or coauthored more than 60 papers in international peer-reviewed journals. His research interests inlude interferometric synthetic aperture radar for mining, permafrost and glacier motion monitoring, especially their 3-D deformation mapping.

Jingxin Hou received the bachelor's degree in surveying and mapping engineering from Central South University, Changsha, China, in 2015. He is currently working toward the Doctoral degree at the Institute of Radar Remote Sensing & Imaging Geodesy (RRSIG), Central South University, Changsha, China.

His research interests include algorithm developments for multitemporal InSAR technique and monitoring deformations of infrastructures in large-scale areas.

Qijie Wang received the Ph.D. degree in astrometry from Shanghai Astronomical Observatory, Chinese Academy of Sciences, Beijing, China, in 2007.

She is a Professor with the School of Geosciences and Info-Physics, Central South University of China, Changsha, China. Her research has been supported by several projects of the National Natural Science Foundation of China. Her main research interests include InSAR deformation monitoring, remote sensing image processing, earth's rotation, and mechanism interpretation. Her current research focuses on tide correction for InSAR deformation monitoring and InSAR monitoring permafrost deformation.